Physics and Chemistry of Minerals (2019) 46:783–793
https://doi.org/10.1007/s00269-019-01039-9

ORIGINAL PAPER

Allanite at high pressure: effect of REE on the elastic behaviour of epidote-group minerals

G. Diego Gatta[1] · Sula Milani[1] · Luca Corti[1] · Davide Comboni[1] · Paolo Lotti[1] · Marco Merlini[1] · Hanns-Peter Liermann[2]

Received: 27 February 2019 / Accepted: 22 May 2019 / Published online: 8 June 2019

Abstract

The compressional behaviour of a natural allanite from Lago della Vecchia (upper Cervo valley, Italy) metagranitoids $[^{A1}(Ca_{0.69}Fe^{2+}_{0.31})_{\Sigma 1.00}{}^{A2}(Ca_{0.46}Ce_{0.24}La_{0.12}Sm_{0.02}Pr_{0.05}Nd_{0.09}Th_{0.02})_{\Sigma 1.00}{}^{M1}(Al_{0.65}Fe^{3+}_{0.34}Ti_{0.02})_{\Sigma 1.01}{}^{M2}(Al_{0.99})^{M3}(Fe^{3+}_{0.54}Fe^{2+}_{0.36}Mg_{0.06}Ti^{4+}_{0.02}Al_{0.01})_{\Sigma 0.99}{}^{Si1,Si2,Si3}(Si_{2.80}Al_{0.20})_{\Sigma 3.00}O_{11}(OH,O)]$ has been investigated up to 16 GPa (at 298 K) by means of in situ synchrotron single-crystal X-ray diffraction. Experiments have been conducted under hydrostatic conditions, using a diamond anvil cell and the mix methanol:ethanol:water = 16:3:1 (up to 10 GPa) and neon (up to 16 GPa) as pressure-transmitting media. No phase transition has been observed within the pressure-range investigated. Data collected in decompression prove that, at least up to 16 GPa (at 298 K), the deformation mechanisms are fully reversible. A third-order Birch–Murnaghan Equation of State (BM-EoS) was fitted to the P–V data (up to 10 GPa), giving: $V_0 = 470.2(2)$ Å^3, $K_{P0,T0} = 131(4)$ GPa and $K' = 1.9(8)$. The evolution of the lattice parameters with pressure shows a slight anisotropic compression pattern, with $K_{P0,T0}(a):K_{P0,T0}(b):K_{P0,T0}(c) = 1.24:1.52:1$. The monoclinic β-angle decreases monotonically with pressure, with: $\beta_P(^\circ) = \beta_{P0} - 0.0902(4)P$ ($R^2 = 0.997$, with P in GPa). The main deformation mechanisms at the atomic scale are described based on a series of structure refinements at different pressures. A comparison between the compressional behavior of allanite, epidote and clinozoisite is carried out.

Keywords Allanite · Epidote · Synchrotron single-crystal X-ray diffraction · High-pressure · Compressibility

Introduction

Allanite is a sorosilicate and a member of the epidote group, with general crystal formula $A(1)A(2)M(1)M(2)M(3)(SiO_4)(Si_2O_7)O(OH)$, where the $A(1)$ and $A(2)$ are sites with coordination number CN > 6 and mainly occupied by Ca, and $M(1)$, $M(2)$ and $M(3)$ are octahedral sites (CN = 6) mainly occupied by Al and Fe^{3+} (Dollase 1971; Franz and Liebscher 2004; Armbruster et al. 2006). All the members of the epidote group are monoclinic in symmetry, with structure topology consistent with the space group $P2_1/m$, although possible symmetry reduction in some epidotes (to Pm, $P2_1$ or $P\bar{1}$) has been suggested as effect of cation ordering (Franz and Liebscher 2004). The structure of the epidote group minerals has single silicate tetrahedra (SiO_4), double silicate tetrahedra (Si_2O_7) and continuous chains of MO_6 and $MO_4(OH)_2$ octahedra (parallel to the b-axis) as main building-block units. The octahedra are bridged by single SiO_4 and double Si_2O_7 tetrahedral groups, in a configuration as that shown in (Fig. 1). Clinozoisite [ideally $^{A1,A2}Ca_2{}^{M1,M2,M3}Al_3(SiO_4)(Si_2O_7)O(OH)$] can be considered as the reference structure of the epidote group minerals, in which the three independent octahedral M sites (*M1*, *M2* and *M3*) are fully occupied by Al and the two independent A sites (*A1* and *A2*) are occupied by Ca. The complex crystal-chemistry of the epidote group led the Commission of the International Mineralogical Association to divide it into three subgroups (Armbruster et al. 2006). The allanite

Electronic supplementary material The online version of this article (https://doi.org/10.1007/s00269-019-01039-9) contains supplementary material, which is available to authorized users.

✉ G. Diego Gatta
diego.gatta@unimi.it

[1] Dipartimento di Scienze della Terra, Università degli Studi di Milano, Via Botticelli 23, 20133 Milan, Italy

[2] Photon Sciences, DESY, PETRA III, Notkestrasse 85, 22607 Hamburg, Germany

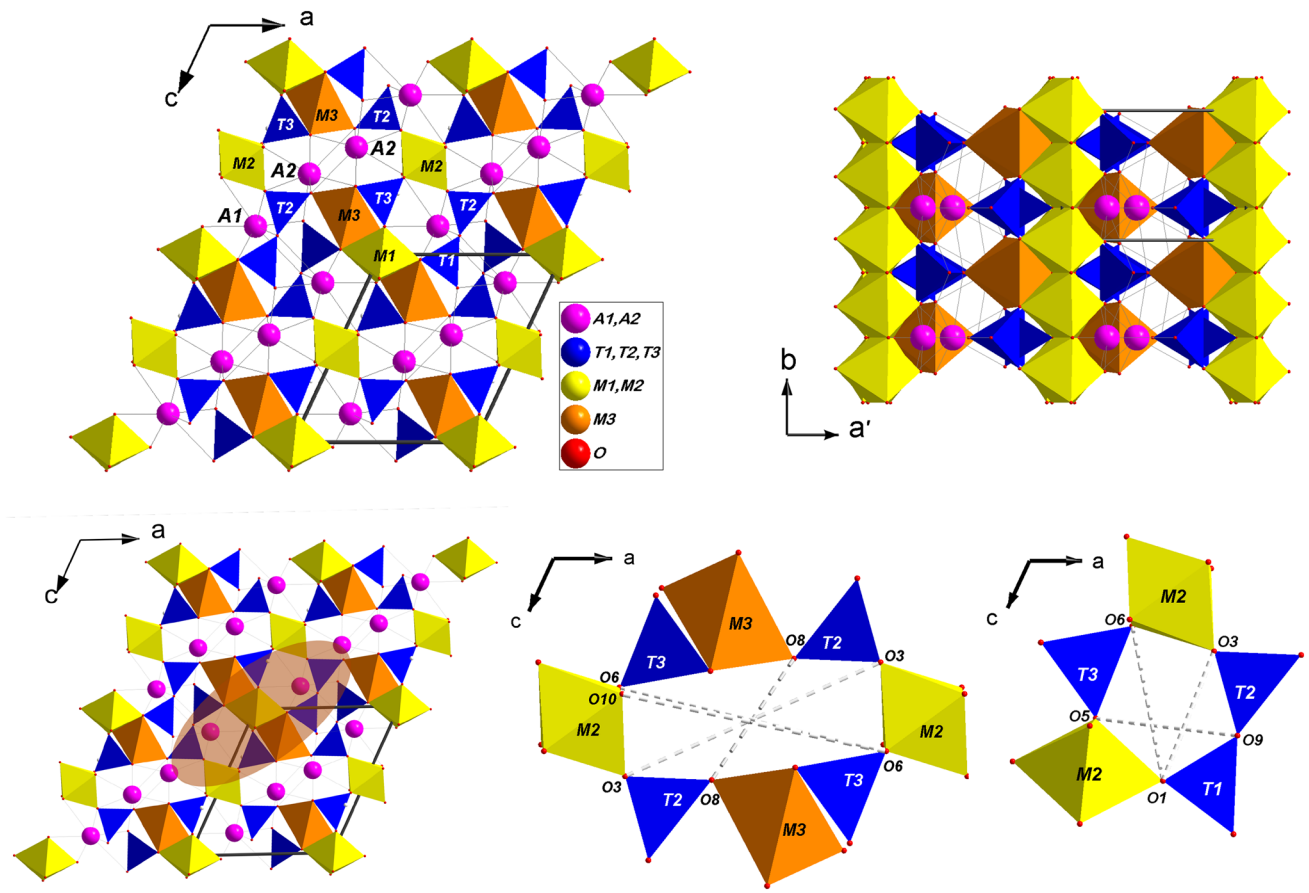

Fig. 1 Crystal structure of allanite viewed down [010] and [001], and overlying unit-strain ellipsoid based on Eulerian finite strain calculated between ambient pressure and 8.51 GPa [$\varepsilon 2//b$, $\varepsilon 1$ and $\varepsilon 3$ lying in the (010)-plane, $\varepsilon 1 \angle a = 136.6(2)°$; $\varepsilon 1 = -0.02849(5)$, $\varepsilon 2 = -0.0192(5)$, and $\varepsilon 3 = -0.01306(8)$/GPa, $\varepsilon 1{:}\varepsilon 2{:}\varepsilon 3 = 2.18{:}1.47{:}1$]. Si-tetrahedra (coordinated by *Si1*, *Si2* and *Si3* sites) and Al/Fe-octahedra (coordinated by the *M1*, *M2* and *M3* sites) are shown as closed-faces polyhedra; large spheres represent the *A1* and *A2*-sites. The 8-membered ring of polyhedra (with the diameters $O3 \leftrightarrow O3$, $O10 \leftrightarrow O6$, $O6 \leftrightarrow O6$ and $O8 \leftrightarrow O8$) and the 5-membered ring (with the diameters $O3 \leftrightarrow O1$, $O1 \leftrightarrow O6$ and $O9 \leftrightarrow O5$) are also shown (see text for further details)

subgroup contains rare-earth elements (REE) rich minerals, typified by the eponymous mineral "allanite". The crystal chemistry of the allanite subgroup members may be derived from that of clinozoisite, by homovalent substitutions and one coupled heterovalent substitution, as follows:

$$^{A2}(\mathrm{REE})^{3+} + {}^{M3}\mathrm{M}^{2+} \rightarrow {}^{A2}\mathrm{Ca}^{2+} + {}^{M3}\mathrm{M}^{3+}$$

In this light, the (cationic) site population is represented by $A1 = \mathrm{M}^{2+}$, $A2 = \mathrm{M}^{3+}$, $M1 = \mathrm{M}^{3+}$, $M2 = \mathrm{M}^{3+}$, and $M3 = \mathrm{M}^{2+}$, and the general formula of allanite is $^{A1}(\mathrm{Ca})^{A2}(\mathrm{REE}^{3+})^{M1,M2}(\mathrm{Al})_2^{M3}(\mathrm{Fe}^{2+})(\mathrm{SiO_4})(\mathrm{Si_2O_7})\mathrm{O(OH)}$ (Dollase 1971; Gieré and Sorensen 2004; Armbruster et al. 2006).

Epidotes mainly occur in low-grade metamorphic rocks (250–400 °C, 1–2 kbars). However, Poli and Schmidt (1998) showed that epidotes are stable over a wide range of pressure and temperature in continental and oceanic crust. Magmatic epidotes were also reported and described by Schmidt and Poli (2004). A series of studies showed how the stability of epidote group minerals is influenced not only by pressure and temperature, but also by the $\mathrm{Al/Fe^{3+}}$ ratio, oxygen fugacity, fluid composition and solution pH (e.g., Holdaway 1972; Liou 1973; Bird and Helgeson 1980; Bird et al. 1988; Klemd 2004). In addition, a series of in situ high-pressure (H*P*) and high-temperature (H*T*) experiments have been devoted to epidote group minerals, and in particular to clinozoisite and epidote sensu stricto, in order to derive volume and axial compressibility or thermal expansion (e.g., Catti et al. 1988; Holland et al. 1996; Pawley et al. 1996; Comodi and Zanazzi 1997; Franz and Liebscher 2004; Liebscher 2004; Gatta et al. 2010, 2011a, b; Qin et al. 2016), along with *P*- or *T*- induced deformation mechanisms at the atomic scale (e.g., Comodi and Zanazzi 1997; Gatta et al. 2010, 2011a). However, to the best of our knowledge, no experiments have so far been devoted to the behaviour of allanite at non-ambient

conditions by in situ experiments. Consequently, bulk and axial compressibilities or thermal expansion coefficients of this mineral are completely unknown, and the role played by the REE replacing Ca at the *A* sites, or the occurrence of Fe^{2+} at the octahedral *M* sites, is still obscure. In this light, the aim of this study was to investigate the H*P*-behaviour of a natural allanite, from Lago della Vecchia (upper Cervo valley, Italy), by in situ synchrotron single-crystal diffraction with a diamond anvil cell, in order to: provide reliable thermodynamic parameters for petrologic modelling, report any potential *P*-induced phase transition and describe the main deformation mechanisms at the atomic scale via single-crystal structure refinements. A comparison between the compressional parameters of allanite and those of epidote sensu stricto and clinozoisite is carried out.

Materials and experimental methods

Natural single-crystals of allanite from Lago della Vecchia (upper Cervo valley, Italy) metagranitoids were used in this study. The host rock is characterized by heterogenous deformation due to strain partitioning (Corti et al. 2017) during development of H*P*–L*T* blueschist-facies dominant fabric, which represents a re-equilibration following the metamorphic peak in the eclogite facies, under thermally depressed conditions (Corti et al. 2018). Chemical microanalyses in wavelength-dispersive mode (EPMA-WDS) were performed on a series of optically homogeneous sub-millimetric crystals, using a JEOL JXA-8200 microprobe at the Earth Sciences Department, University of Milano. The system was operated using an accelerating voltage of 15 kV, a beam current of 5 nA, a beam diameter of 5 µm, and a counting time of 30 s on the peaks and 10 s on the backgrounds. A series of natural and synthetic standards were used. The raw data were corrected for matrix effects using the protocol implemented in the JEOL suite of programs. The crystals of allanite, selected for this study, were found to be compositionally homogeneous. The average unit-formula, based on more than 40 point-analyses and calculated following the protocol recommended by the IMA Commission (Armbruster et al. 2006), on the basis of 13 oxygen atoms, is: $^{A1}(Ca_{0.69}Fe^{2+}_{0.31})_{\Sigma1.00}{}^{A2}(Ca_{0.46}Ce_{0.24}La_{0.12}Sm_{0.02}Pr_{0.05}Nd_{0.09}Th_{0.02})_{\Sigma1.00}{}^{M1}(Al_{0.65}Fe^{3+}_{0.34}Ti_{0.02})_{\Sigma1.01}{}^{M2}(Al_{0.99})^{M3}(Fe^{3+}_{0.54}Fe^{2+}_{0.36}Mg_{0.06}Ti^{4+}_{0.02}Al_{0.01})_{\Sigma0.99}{}^{Si1,Si2,Si3}(Si_{2.80}Al_{0.20})_{\Sigma3.00}O_{11}(OH,O)$. Further details pertaining to experimental protocols and EPMA-WDS data statistics will be published elsewhere.

High-pressure synchrotron X-ray single-crystal diffraction experiments were performed at the Extreme Conditions Beamline P02.2 at DESY/PETRAIII. X-rays with an energy of 42.7 keV (0.2904 Å wavelength) were used, with a focusing spot of ~ 8.5 (H) × 1.8 (V) μm^2 originating from a compound refractive lense (CRL) system consisting of 111 Be lenses with a radius of 50 µm (400 µm beam acceptance) and a focal length of 1221 mm. Two prismatic single-crystals of allanite (~ 50 × 50 × 15 μm^3) were selected for the H*P* experiments, loaded, respectively, in two symmetric diamond anvil cells (DAC), equipped with Boehler–Almax design diamonds/seats with a 70° opening and 300-µm culets size. For the first DAC, a 250-µm-thick rhenium gasket was pre-indented to 50 µm and then drilled with 150 µm hole, in which the crystal of allanite, along with some calibrated ruby spheres (for pressure determination, according to Mao et al. 1986), were placed. Neon was used as hydrostatic pressure-transmitting medium (Klotz et al. 2009). For the second DAC, a 250-µm-thick steel gasket was pre-indented to 60 µm and then drilled with 150 µm hole, in which the crystal of allanite and ruby micro-spheres were located. In this case, the methanol:ethanol:water = 16:3:1 mix was used as hydrostatic *P*-transmitting fluid up to 10 GPa (Angel et al. 2007). For both the experiments, pressure was increased with an automated pressure-driven system and measured with the online ruby/alignment system. Diffraction images were acquired on a PerkinElmer XRD 1621 flat panel detector, using an in-house script for collecting step-scan diffraction images. Sample to detector distance (402.34 mm) was calibrated using a CeO_2 standard (NIST 674a). The diffraction images were then converted to conform to the "Esperanto" format of the program CrysAlis (Rigaku–Oxford Diffraction 2018; Rothkirch et al. 2013). The diffraction data were first collected with the crystals in the DAC and without any *P*-transmitting medium (i.e. ambient pressure). A pure ω-scan ($-33° \le \omega \le +33°$), with a step size of 0.5° and an exposure time of 1 s/frame, was used during data collection. X-ray diffraction peaks were then indexed and their intensities were integrated and corrected for Lorentz-polarization (Lp) effects, using the CrysAlis™ package. Scaling and correction for absorption (due to the DAC components) was applied by the semi-empirical *ABSPACK* routine implemented in CrysAlis. The reflection conditions were consistent with those of the space group $P2_1/m$. H*P* data for the experiments with methanol:ethanol:water mix as *P*-transmitting fluid were collected up to ~ 8.5 GPa; those pertaining to the experiment with neon as *P*-transmitting medium up to ~ 16.3 GPa (the hydrostatic limit of neon, according to Klotz et al. 2009). No evidence of phase transitions was observed within the *P*-range investigated. Data collected in decompression proved that allanite behaves elastically at least up to 16 GPa (at 298 K) (Table 1) under hydrostatic conditions. The unit-cell parameters of allanite with *P*, based on the two different ramps (i.e., in methanol:ethanol:water mix and in neon) are listed in Table 1.

The isotropic structure refinements, based on the intensity data of the two H*P* ramps, were conducted using the software SHELXL97 (Sheldrick 1997, 2008), starting from the

Table 1 Lattice parameters of allanite at different pressures, based on the two datasets collected using the methanol:ethanol:water mix (H*P*-mew) and neon (H*P*-Ne) as *P*-transmitting fluids (*P* uncertainty: ±0.1 GPa)

Experiment	*P* (GPa)	*a* (Å)	*b* (Å)	*c* (Å)	*β* (Å)	*V* (Å^3)
H*P*-mew[a]	0.0001	8.9116(3)	5.738(2)	10.1447(4)	114.979(4)	470.2(2)
H*P*-mew[b]	0.0001	8.9130(2)	5.735(2)	10.1484(3)	114.993(3)	470.2(2)
H*P*-mew	1.17	8.8882(4)	5.719(2)	10.1071(4)	114.872(6)	466.1(2)
H*P*-mew	1.60	8.8781(4)	5.712(2)	10.0911(3)	114.832(5)	464.42(9)
H*P*-mew	1.97	8.8718(4)	5.707(2)	10.0821(4)	114.805(5)	463.4(1)
H*P*-mew	2.81	8.8497(2)	5.697(8)	10.0509(2)	114.707(3)	460.33(7)
H*P*-mew	3.30	8.8416(4)	5.6890(2)	10.0383(4)	114.684(5)	458.8(1)
H*P*-mew	3.61	8.8325(3)	5.6880(9)	10.0293(3)	114.647(3)	457.96(7)
H*P*-mew	3.99	8.8223(2)	5.6834(8)	10.0152(2)	114.593(3)	456.62(7)
H*P*-mew	4.86	8.7996(3)	5.674(1)	9.9865(3)	114.519(4)	453.63(8)
H*P*-mew	5.08	8.7963(2)	5.6686(9)	9.9813(2)	114.512(3)	452.84(7)
H*P*-mew	5.55	8.7851(2)	5.6657(9)	9.9667(2)	114.462(3)	451.55(7)
H*P*-mew	6.45	8.7655(2)	5.6550(9)	9.9412(2)	114.388(3)	448.80(7)
H*P*-mew	7.07	8.7466(3)	5.644(2)	9.9177(3)	114.321(4)	446.2(1)
H*P*-mew	7.61	8.7384(3)	5.638(2)	9.9073(3)	114.287(4)	444.94(9)
H*P*-mew	8.51	8.7231(3)	5.629(2)	9.8817(3)	114.225(4)	442.50(9)
H*P*-Ne[c]	1.39	8.8881(6)	5.7303(3)	10.111(2)	114.88(2)	467.2(2)
H*P*-Ne[c]	9.90	8.668(3)	5.6171(2)	9.839(6)	113.87(6)	438.1(3)
H*P*-Ne[c]	14.64	8.563(3)	5.5643(2)	9.722(7)	113.56(7)	424.6(4)

[a]Sample in the DAC without *P*-medium

[b]After decompression

[c]For the experiments in Ne, the *P* value at any data point represents the average value obtained by the ruby-fluorescence method and the BM-EoS fit based on the mew experiments

structure model of Dollase (1971) and Bonazzi et al. (2009), in the space group $P2_1/m$. To reduce the number of variables to refine, and considering the average chemical composition of the allanite of this study, the atomic sites were modelled as follows: the *A1* and *A2* sites were modelled with a mixed (Ca + Ce) X-ray scattering curve, and the fractions of Ca vs. Ce were refined; the *M1* and *M2* octahedral sites as populated by Al only and the *M3* site as populated by (Fe + Al), and the fractions Fe vs. Al were refined; the three independent tetrahedral sites (i.e., *Si1*, *Si2* and *Si3*) were modelled as fully occupied by Si. For all the refinements, convergence was rapidly achieved and, at the end of the last cycles of refinement, no significant correlation was observed in the variance–covariance matrix of the refined parameters. The principal statistical parameters of the structure refinements are listed in Table 2. Atomic coordinates and site occupancies of selected structure refinements are given in Table S1. Bond distances and other relevant structural parameters are reported in Tables S2 and 3.

Results: elastic behaviour of allanite at high-pressure

The evolution of the lattice parameters of allanite with pressure is shown in Fig. 2 and Fig. S1, which shows that no phase transition or change of the deformation mechanisms occur within the *P*-range investigated (i.e., at least up to 16 GPa at 298 K). A second- and a third-order Birch–Murnaghan Equations of State (BM-EoS) (Birch 1947; Angel 2000) were fitted to the *P*–*V* data pertaining to the experiment with methanol:ethanol:water mix as *P*-transmitting fluid (i.e., the most populated *P* ramp), using the EOS-FIT program (by RJ Angel, www.rossangel.com). This isothermal EoS is based on the assumption that the high-pressure strain energy in a solid can be expressed as a Taylor series in the Eulerian finite strain, defined as $fe = [(V_0/V)^{2/3} - 1]/2$, and allows to obtain the bulk modulus ($K_{P0,T0} = V(\partial P/\partial V)_{T0} = \beta^{-1}_{P0,T0}$, where $\beta_{P0,T0}$ is the volume compressibility coefficient at room conditions) and its *P*-derivatives. Expansion in the Eulerian strain polynomial has the following form:

$$P(fe) = 3K_{P0,T0}fe(1 + 2fe)^{5/2}\{1 + 3/2(K' - 4)fe + 3/2[K_{P0,T0}K'' + (K' - 4)(K' - 3) + 35/9]fe^2 + \cdots\},$$
$$\text{where } K' = \partial K_{P0,T0}/\partial P \text{ and } K'' = \partial^2 K_{P0,T0}/\partial P^2$$

The BM-EoS parameters, simultaneously refined using the data weighted by their uncertainties in *P* and *V,* are listed in Table 4. Using a second-order BM-EoS fit, convergence is achieved with: $V_0 = 470.6(2)$ Å^3 and $K_{P0,T0} = 122(1)$ GPa.

Table 2 Details pertaining to selected data collections and structure refinements of allanite at different pressures (*P* uncertainty: ±0.1 GPa)

P (GPa)	0.0001[a]	1.17	1.60	1.97	3.61	3.99	4.86	5.08	5.55	6.45	7.07	7.61	8.51	1.39[b]	9.90[b]	14.64[b]
a (Å)	8.9116(3)	8.8882(4)	8.8781(4)	8.8718(4)	8.8325(3)	8.8223(2)	8.7996(3)	8.8223(2)	8.7996(3)	8.7655(2)	8.7466(3)	8.7384(3)	8.7231(3)	8.8881(6)	8.668(3)	8.563(3)
b (Å)	5.738(2)	5.719(2)	5.712(2)	5.707(2)	5.6880(9)	5.6834(8)	5.674(1)	5.6834(8)	5.674(1)	5.6550(9)	5.644(2)	5.638(2)	5.6475(2)	5.7303(3)	5.6171(2)	5.5643(2)
c (Å)	10.1447(4)	10.1071(4)	10.0911(3)	10.0821(4)	10.0293(3)	10.0152(2)	9.9865(3)	10.0152(2)	9.9865(3)	9.9412(2)	9.9177(3)	9.9073(3)	9.8817(3)	10.111(2)	9.839(6)	9.722(7)
β (Å)	114.979(4)	114.872(6)	114.832(5)	114.805(5)	114.647(3)	114.593(3)	114.519(4)	114.593(3)	114.519(4)	114.388(3)	114.321(4)	114.287(4)	114.225(4)	114.88(2)	113.87(6)	113.56(7)
V (Å^3)	470.2(2)	466.1(2)	464.42(9)	463.4(2)	457.96(7)	456.62(7)	453.63(8)	456.62(7)	453.65(8)	448.80(7)	446.2(1)	444.94(9)	445.2(3)	467.2(2)	438.1(3)	424.6(4)
Space group	$P2_1/m$	$P2_1/m$	$P2_1/m$	$P2_1/m$	$P2_1/m$	$P2_1/m$	$P2_1/m$	$P2_1/m$	$P2_1/m$	$P2_1/m$	$P2_1/m$	$P2_1/m$	$P2_1/m$	$P2_1/m$	$P2_1/m$	$P2_1/m$
λ (Å)	0.28940	0.28940	0.28940	0.28940	0.28940	0.28940	0.28940	0.28940	0.28940	0.28940	0.28940	0.28940	0.28940	0.28940	0.28940	0.28940
θ_{max} (°)	18.08	17.99	18.01	18.02	18.1	18.11	18.15	18.11	18.15	17.93	17.97	17.98	18.02	18.11	17.43	17.63
No. measured reflections	2272	2147	2186	2127	2137	2170	2020	2170	2020	1980	1834	2067	2158	1657	1432	1494
No. unique reflections	1106	1189	1185	1168	1148	1135	1059	1135	1059	1064	985	1053	1078	946	741	724
No. unique reflections with $F_o > 4\sigma(F_o)$	1106	1189	1185	1168	1148	1135	1059	1135	1059	1064	985	1053	1076	945	736	723
No. refined parameters	66	63	63	63	63	63	63	63	63	63	63	63	63	63	63	64
R_{int}	0.0159	0.0189	0.0203	0.0221	0.0274	0.0207	0.0172	0.0207	0.0172	0.0232	0.0225	0.019	0.0209	0.0176	0.0244	0.0215
R_1 (F) with $F_o > 4\sigma(F_o)$	0.0356	0.0351	0.0396	0.0466	0.0452	0.0403	0.0404	0.0403	0.0404	0.0421	0.0498	0.0385	0.0377	0.0442	0.0609	0.0479
wR_2 (F^2)	0.0952	0.0931	0.1046	0.122	0.1229	0.1021	0.1057	0.1021	0.1057	0.1072	0.1206	0.1	0.0985	0.1107	0.1523	0.1195
GooF	1.319	1.198	1.326	1.509	1.447	1.325	1.387	1.325	1.387	1.331	1.481	1.350	1.302	1.480	1.970	1.601
Residuals (e$^-$/Å^3)	−0.86/+ 1.01	−0.77/+ 1.12	−1.06/1.16	−1.12/1.30	−1.27/1.50	−1.34/1.03	−1.45/1.13	−1.34/1.03	−1.45/1.13	−1.35/1.02	−1.51/0.96	−1.10/1.06	−1.21/1.21	−1.38/1.03	−1.47/1.70	−1.03/1.23

[a]Sample in the DAC without *P* medium. The Ca vs. Ce fractions at the *A1* and *A2* sites and the Al vs. Fe fraction at the *M3* site were refined at 0.0001 GPa and then kept fixed at higher pressure

[b]Neon used as pressure-transmitting medium

Table 3 Principal "diameters" (Å) of the 8-membered ring of polyhedra (*O6*↔*O10*, *O3*↔*O3*, *O6*↔*O6* and *O8*↔*O8*) and of the 5-membered one (*O3*↔*O1*, *O6*↔*O1*, *O9*↔*O5*) at different pressures (*P* uncertainty: ±0.1 GPa)

Experiment	*P* (GPa)	*O6*↔*O10*	*O3*↔*O3*	*O6*↔*O6*	*O8*↔*O8*	*O3*↔*O1*	*O6*↔*O1*	*O9*↔*O5*
H*P*-mew[a]	0.0001	7.032(9)	7.297(10)	7.702(9)	4.778(8)	3.615(5)	4.364(11)	4.674(5)
H*P*-mew	1.17	7.011(10)	7.251(14)	7.677(7)	4.707(8)	3.606(5)	4.352(15)	4.672(5)
H*P*-mew	1.60	7.005(9)	7.251(12)	7.668(7)	4.691(9)	3.601(5)	4.349(13)	4.669(5)
H*P*-mew	1.97	7.001(12)	7.245(10)	7.660(9)	4.682(11)	3.596(6)	4.347(13)	4.672(6)
H*P*-mew	3.61	6.971(8)	7.198(8)	7.637(9)	4.624(10)	3.581(5)	4.338(9)	4.671(6)
H*P*-mew	3.99	6.968(7)	7.184(8)	7.631(7)	4.619(9)	3.579(5)	4.337(9)	4.655(5)
H*P*-mew	4.86	6.951(9)	7.162(10)	7.612(9)	4.587(9)	3.571(5)	4.332(11)	4.652(5)
H*P*-mew	5.08	6.948(8)	7.159(8)	7.612(9)	4.581(10)	3.568(5)	4.334(9)	4.657(6)
H*P*-mew	5.55	6.942(8)	7.146(8)	7.610(9)	4.560(10)	3.563(5)	4.326(9)	4.651(6)
H*P*-mew	6.45	6.925(8)	7.131(8)	7.592(9)	4.538(9)	3.554(5)	4.321(9)	4.649(6)
H*P*-mew	7.07	6.912(10)	7.119(11)	7.579(10)	4.515(11)	3.543(6)	4.314(12)	4.644(7)
H*P*-mew	7.61	6.901(8)	7.114(10)	7.566(9)	4.502(9)	3.539(4)	4.314(11)	4.644(5)
H*P*-mew	8.51	6.883(8)	7.101(10)	7.547(7)	4.478(9)	3.531(4)	4.309(11)	4.643(5)

[a]Sample in the DAC without *P* medium

A better fit is obtained using a third-order BM-EoS with $V_0 = 470.2(2)$ Å^3, $K_{P0,T0} = 131(4)$ GPa and $K' = 1.9(8)$. The use of a third-order BM-EoS in energy, to model the compressional behaviour of allanite, is also corroborated by the evolution of the Eulerian finite strain vs. "normalized stress" plot (*fe–Fe* plot, with $Fe = P/[3fe(1+2fe)^{5/2}]$; Angel 2000), shown in Fig. 3: the weighted linear regression through the data points yields $Fe(0) = 131(2)$ GPa as intercept value and the (negative) slope of the regression line gives rise to a K' value of 1.9(6), in good agreement with the third-order BM-EoS fit.

The confidence ellipses at 68.3% level ($\Delta\chi^2 = 2.30, \pm 1\sigma$), 95.4% level ($\Delta\chi^2 = 6.17, \pm 2\sigma$) and 99.7% level ($\Delta\chi^2 = 11.8, \pm 3\sigma$) were calculated starting from the variance–covariance matrix of $K_{P0,T0}$ and K' obtained from the least-square procedure (third-order BM-EoS fit previously described; Angel 2000). The ellipses are strongly elongated with negative slope (Fig. 4), showing a negative correlation of the parameters $K_{P0,T0}$ and K'.

The evolution of the lattice parameters with pressure shows a slight anisotropic compressional pattern. The "axial bulk moduli", calculated with a second-order "linearized" BM-EoS (Angel 2000 for details), are $K_{P0,T0}(a) = 114(2)$ GPa for the *a*-axis, $K_{P0,T0}(b) = 140(4)$ GPa for the *b*-axis, and $K_{P0,T0}(c) = 92(1)$ GPa for the *c*-axis, with a general anisotropic compressional scheme: $K_{P0,T0}(a):K_{P0,T0}(b):K_{P0,T0}(c) = 1.24:1.52:1$ (Table 4). The second-order BM-EoS fits provide the best figure of merit. The monoclinic β-angle decreases linearly with pressure, with: $\beta_P\,(^\circ) = \beta_{P0}\,(^\circ) - 0.0902\,(4)P$ ($R^2 = 0.997$, with *P* in GPa) (Fig. 2 and S1).

Magnitude and orientation of the principal unit-strain coefficients between room pressure and the maximum *P* achieved (i.e., $\Delta P = 8.51$ GPa, ramp in methanol:ethanol:water mix), derived on the basis of the finite Eulerian strain tensor, were calculated with the *Win_Strain* software (by RJ Angel, www.rossangel.com). The following cartesian axial system was chosen: *x*//*a** and *y*//*b*. The strain ellipsoid is oriented with the mid axis ($\varepsilon 2$) parallel to the *b*-axis, and the major ($\varepsilon 1$) and minor ($\varepsilon 3$) axes lying in the (010)-plane: $\varepsilon 1$ describes an angle of 136.6(2)° from *a* (and thus 22.3(2)° from *c*), as shown in Fig. 1. The elastic behaviour of allanite based on the unit-strain coefficients between 0.0001 and 8.51 GPa is more anisotropic if compared to that deduced only along the principal crystallographic directions, being $\varepsilon 1 = -0.02849(5)$, $\varepsilon 2 = -0.0192(5)$, and $\varepsilon 3 = -0.01306(8)$ GPa^{-1}, with the resulting anisotropic scheme: $\varepsilon 1{:}\varepsilon 2{:}\varepsilon 3 = 2.18{:}1.47{:}1$.

As only a few data-points were collected in Ne (Tables 1 and 2), such an experiment was mainly aimed to demonstrate that, at least up to 16 GPa, allanite is still crystalline. Thus, Ne-data were not used for the compressional analysis.

Results: deformation mechanisms at the atomic scale

The mechanisms at the atomic scale that govern the anisotropic compression of the allanite structure can be described in terms of intra- and inter-polyhedral re-arrangement in response to the applied pressure. Intra-polyhedral deformations are usually described in terms of compression of the bond distances or by distortion (i.e., with or without bond-distances compression), inter-polyhedral rearrangements in terms of polyhedral tilting.

If we consider the *P*-induced atomic displacements in allanite structure, the oxygen sites *O8* and *O9* show the most pronounced displacements from their positions refined at 0.0001 GPa. *O9* is the bridging oxygen between the *T1* and

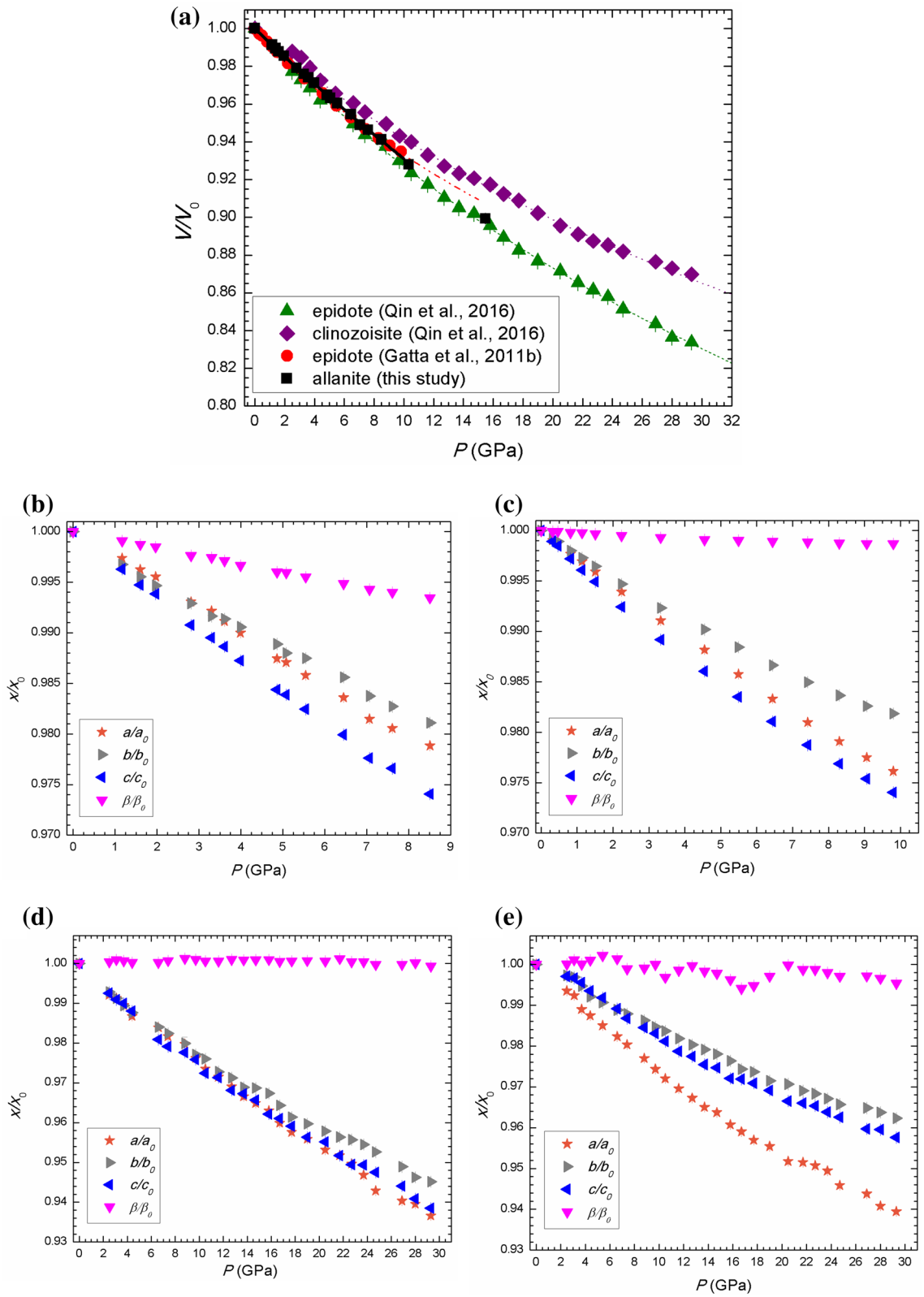

Fig. 2 Evolution of the lattice parameters of allanite with *P* (GPa). **a** For the unit-cell volume, the solid lines represent the third-order BM-EoS fits. The axial compressional behaviours of **b** allanite (this study), **c** epidote with 0.74 Fe a.p.f.u. (Gatta et al. 2011b), **d** epidote with 0.79 Fe a.p.f.u. (Qin et al. 2016), and **e** clinozoisite with 0.40 Fe a.p.f.u. (Qin et al. 2016) are also shown

Table 4 Compressional parameters of allanite obtained by second- and third-order Birch–Murnaghan Equation of State fits (see text for details)

	V_0, l_0 (Å^3, Å)	$K_{P0,T0}$ (GPa)	K'	*EoS* order
V_0	470.6(2)	122(1)	4 (fixed)	2nd order
a_0	8.918(3)	114(2)	4 (fixed)	2nd order
b_0	5.735(2)	140(4)	4 (fixed)	2nd order
c_0	10.149(2)	92(1)	4 (fixed)	2nd order
V_0	470.2(2)	131(4)	1.9 (8)	3rd order

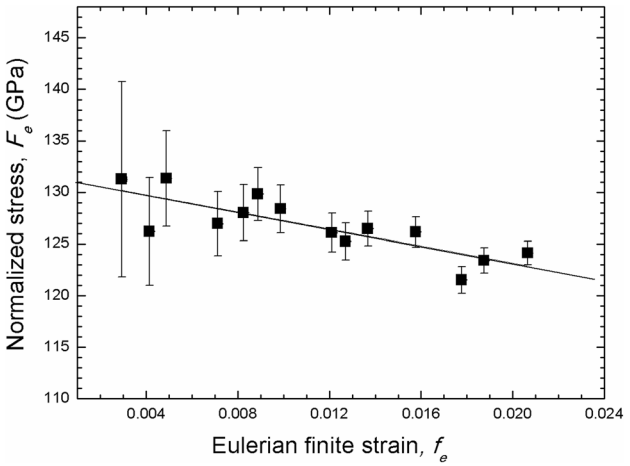

Fig. 3 Normalized stress ($Fe = P/[3fe(1+2fe)^{5/2}]$) vs. Eulerian finite strain ($fe = [(V_0/V)^{2/3} - 1]/2$) plot. The *e.s.ds* have been calculated according to Heinz and Jeanloz (1984). The solid line is a weighted linear fit through the data

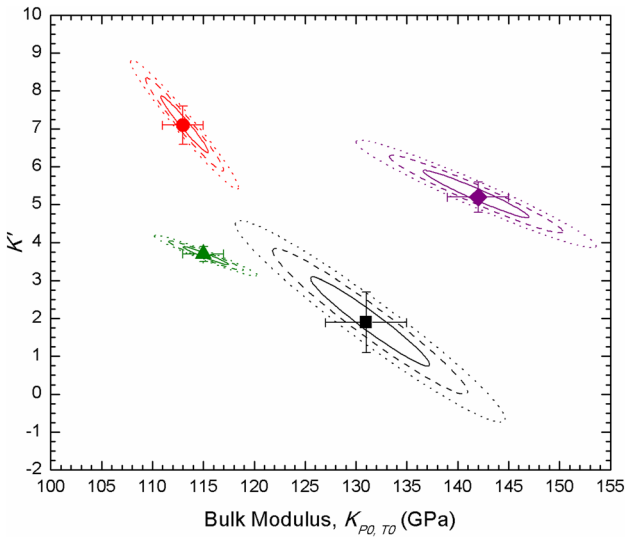

Fig. 4 Confidence ellipses at 68.3% level ($\Delta\chi^2 = 2.30, \pm 1\sigma$, solid black line), 95.4% level ($\Delta\chi^2 = 6.17, \pm 2\sigma$, dashed black line) and 99.7% level ($\Delta\chi^2 = 11.8, \pm 3\sigma$, dotted black line) calculated starting from the variance–covariance matrix of $K_{P0,T0}$ and K' obtained from the BM-EoS least-square procedure of this study on allanite. The $K_{P0,T0}$ and K' of Gatta et al. (2011b) for epidote (0.74 Fe a.p.f.u.; red circle), of Qin et al. (2016) for epidote (0.79 Fe a.p.f.u.; dark green triangle), and of Qin et al. (2016) for clinozoisite (0.40 Fe a.p.f.u.; purple diamond) are added for comparison (see text for further details). Error bars: ± 1 *e.s.ds*

T2 tetrahedra, describing the angle *T1*-*O9*-*T2* of ~ 145.5° at 0.0001 GPa, which decreases to ~ 140.4° at 8.5 GPa (Table S2); the difference is remarkable, if we consider the *P*-range. This tilting mechanism, governed by the displacement of the *O9* site, affects the shape of the 5-membered rings of polyhedra (*M2*–*T3*–*M2*-*T2*–*T1*, Fig. 1), confining the cavities in which the *A1* site lies: the contraction of the *O*3↔*O*1, *O*6↔*O*1 and *O*9↔*O*5 "diameters" is significatly different, being, respectively, ~ 0.09, ~ 0.06, and ~ 0.03 Å within the *P*-range 0.0001–8.5 GPa (Fig. 5). *O9* is also bonded to the *A1* site, and the displacement of the *O*9 leads to a change of the *A1*–*O*9 bond length: ~ 3.095 Å at 0.0001 GPa and ~ 3.074 Å at 8.5 GPa (Table S2).

O8 is the bridging oxygen between the *T2* and *M3* polyhedra. The *T2*–*O8*–*M3* angle is ~ 130.3º at 0.0001 GPa and drastically decreases to ~ 123.0º at 8.5 GPa (Table S2). The displacement of the *O8* site and the aforementioned and co-related polyhedral tilting affect the shape evolution with *P* of the 8-membered rings of polyhedra (*M2*–*T3*–*M3*–*T2*–*M2*–*T3*–*M3*–*T2*), in which the *A2* site lies (Fig. 1). More specifically, the *O*8↔*O*8 "diameter" is pronouncedly shortened by ~ 0.30 Å at 8.51 GPa and, in the same *P*-range, the *O*3↔*O*3, *O*6↔*O*10 and *O*6↔*O*6 diameters are shortened by ~ 0.20, ~ 0.15, and ~ 0.16 Å, respectively (Figs. 1 and 5, Table 3). This leads to a more rectangular-edged ring at high pressure, affecting mainly the length of the unit-cell edge parallel to the *c*-axis.

The aforementioned polyhedral tilting mechanisms are coupled with the intra-polyhedral distortion and compression in response to the applied pressure, which are energetically costly and, therefore, less pronounced at low- or mid-*P* regimes. The evolution of the intra-polyhedral bond distances and angles shows that, within the *P*-range investigated, tetrahedra behaves as quasi-rigid units at a first approximation (with minor bond-distances shortening or polyhedral distortion), octahedra are more affected by compression and distortion (though not dramatic), whereas the large *A1*- and *A2*-polyhedra are the most affected by distortion and bond-distances shortening in response to the applied pressure (Table S2). However, the quality of the structural data at high pressure allows us to observe a different behaviour among the three independent tetrahedra: *T1* and *T2* are essentially rigid (i.e., difference in their bong lengths of the same order of the *e.s.ds*), but *T3* tends to deform significantly, in particular in response to the shortening of the *T3*–*O2* distance of about 0.03 Å (with $\Delta P = 8.5$ GPa; Table S2). Even among the three independent octahedra, we can observe different magnitude

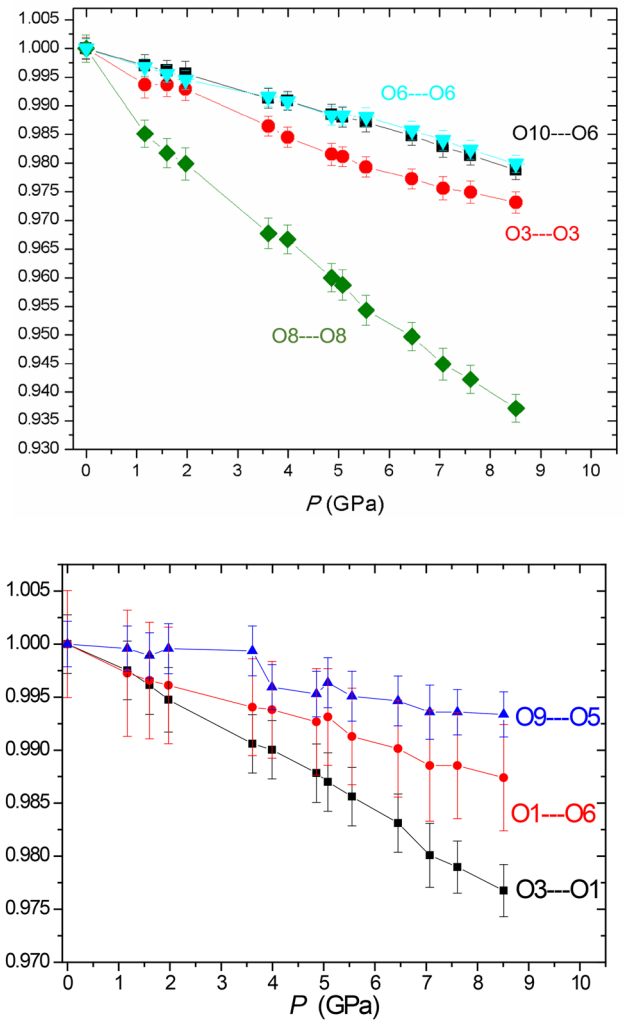

Fig. 5 Evolution with *P* of the (normalised) *O*3↔*O*3, *O*6↔*O*6, *O*8↔*O*8 and *O*10↔*O*6 "diameters" of the 8-membered ring of polyhedra, and of the *O*3↔*O*1, *O*1↔*O*6 and *O*9↔*O*5 "diameters" of the 5-membered ring (see Fig. 1 and text for further details)

of compression + distortion: within the *P*-range investigated, the maximum shortening of the intra-polyhedral bond lengths is ~ 0.04 Å for the *M2* octahedron, ~ 0.06 Å for the *M1* octahedron, and ~ 0.10 Å for the *M3* octahedron. Therefore, the Fe-rich *M3* octahedron is the most distorted one under hydrostatic compression, even in response to the pronounced *T2–O8–M3* compression described above.

One open question concerns the role played by the H-bonding scheme on the *P*-induced structure evolution of allanite. In allanite structure (as in all the epidote-group members), there is only one unique *H* site. *O*10 acts as *donor* and *O*4 acts as *acceptor* of the H-bond (i.e., *O*10–*H*…*O*4); *O*4 is the oxygen co-shared by two *M1* and one *M3* octahedra and *O*10 is the bridging oxygen between the edge-sharing *M2* octahedra. Proton, donor and acceptor are confined in the 5-membered ring of polyhedra (Fig. 1).

It is impossible to refine the *H* site coordinates in the H*P* structure refinements. However, we can intuitively consider that the H-bonding geometry can explain why in the 5-membered ring the major deformation mechanism acts on one side through the *T1*–O9–*T2* tilting, as the *T1* and *T2* tetrahedra are unaffected by the H-bonding. As a consequence, the *O*3↔*O*1 shortening is more pronounced than the *O*6↔*O*1 and *O*9↔*O*5 ones (Fig. 1, Tables S2 and 3).

Discussion and conclusions

To the best of our knowledge, this is the first study on the compressional behaviour of allanite, here described on the basis of in situ synchrotron single-crystal diffraction data. The experimental findings of this study confirm that allanite preserves its crystallinity and behaves elastically at least up to 16 GPa (at 298 K), under hydrostatic compression (Table 2).

The Eulerian unit-strain ellipsoid, calculated between 0.0001 and 8.51 GPa, confirms that the lowest and the highest compression directions lie on the (010)-plane, as shown in Fig. 1: the softest direction ($\varepsilon1$) describes an angle of 136.6(2)° from [100], and, as a consequence, the stiffest direction ($\varepsilon3$) describes an angle of 46.6(2)° from [100]. A recalculation of magnitude and orientation of the compressional unit-strain ellipsoids of epidote with 0.74 Fe a.p.f.u. (based on the data of Gatta et al. 2011b, for $\Delta P = 8.30$ GPa, $P_{min} = 0.0001$ GPa), of epidote with 0.79 Fe a.p.f.u. (based on the data of Qin et al. 2016, for $\Delta P = 9.70$ GPa, $P_{min} = 0.0001$ GPa), and clinozoisite with 0.40 Fe a.p.f.u. (based on the data of Qin et al. 2016, for $\Delta P = 8.80$ GPa, $P_{min} = 0.0001$ GPa), was done, using the same cartesian axial system and strain definition (i.e., Eulerian) adopted for allanite:

(1) In epidote with 0.79 Fe a.p.f.u., the stiffest direction ($\varepsilon3 = -0.0232(2)$/GPa) is parallel to [010], whereas the mid ($\varepsilon2 = -0.0236(3)$/GPa) and the softest ($\varepsilon1 = -0.0258(8)$/GPa) directions lie on (010), with the softest one describing an angle of 63(5)° with [100]; anisotropic compressional scheme: $\varepsilon1:\varepsilon2:\varepsilon3 = 1.11:1.01:1$, i.e. there is an almost circular section of the ellipsoid in which $\varepsilon2$ and $\varepsilon3$ are dispersed; the monoclinic β angle decreases monotonically with *P* (Qin et al. 2016);
(2) In epidote with 0.74 Fe a.p.f.u., the stiffest direction ($\varepsilon3 = -0.01646(8)$/GPa) is parallel to [010], whereas the mid ($\varepsilon2 = -0.01978(8)$/GPa) and the softest ($\varepsilon1 = -0.02352(6)$/GPa) directions lie on (010), with the softest one describing an angle of 126.7(8)° with [100]; anisotropic compressional

scheme: $\varepsilon1$:$\varepsilon2$:$\varepsilon3$ = 1.43:1.20:1; the monoclinic β angle decreases monotonically with P (Gatta et al. 2011b);

(3) In clinozoisite (0.40 Fe a.p.f.u.), the stiffest direction ($\varepsilon3 = -0.0138(2)$/GPa) is parallel to [010], whereas the mid ($\varepsilon2 = -0.0145(2)$/GPa) and the softest ($\varepsilon1 = -0.0234(1)$/GPa) directions lie on (010), with the softest one describing an angle of 174(1)° with [100]; anisotropic compressional scheme: $\varepsilon1$:$\varepsilon2$:$\varepsilon3$ = 1.70:1.05:1; the monoclinic β angle decreases monotonically with P (Qin et al. 2016).

On this basis, some general conclusions can be drawn:

(1) The softest directions in allanite, epidote(s) and clinozoisite lie all on (010);
(2) The stiffest directions in epidote and clinozoisite are consistently oriented parallel to [010], whereas in allanite it lies on (010) [i.e., $\varepsilon3 \angle [100] = 46.6(2)°$];
(3) The compressional schemes of allanite, epidote(s) and clinozoisite are significantly different: more anisotropic in allanite ($\varepsilon1$:$\varepsilon2$:$\varepsilon3$ = 2.18:1.47:1), less in epidote ($\varepsilon1$:$\varepsilon2$:$\varepsilon3$ = 1.43:1.20:1 with 0.74 Fe a.p.f.u, and $\varepsilon1$:$\varepsilon2$:$\varepsilon3$ = 1.11:1.01:1 with 0.79 Fe a.p.f.u) and clinozoisite ($\varepsilon1$:$\varepsilon2$:$\varepsilon3$ = 1.70:1.05:1);
(4) Concerning the joint epidote-clinozoisite, a drastic rotation of the unit-strain ellipsoid in response to the different Fe content is observable: the softest direction describes an angle from [100] of 174(1)° in clinozoisite with 0.40 Fe a.p.f.u., of 126.7(8)° in epidote with 0.74 Fe a.p.f.u. and of 63(5)° in epidote with 0.79 Fe a.p.f.u., i.e. the lower the Fe content, the higher the angle $\varepsilon1 \angle [100]$.

The stiffest direction can easily assume a different orientation in response to small compositional changes, due to the modest anisotropy observed ($\varepsilon2$:$\varepsilon3$ = 1.01:1 and 1.20:1 in epidote, 1.05:1 in clinozoisite, and 1.47:1 in allanite).

Our data on allanite show that the inter- and intra-polyhedral mechanisms, described on the basis of the structure refinements at high pressure, are not sufficient to explain, unambiguously, magnitude and orientation of the unit-strain ellipsoid. In this light, only some general considerations can be done:

(1) The Eulerian unit-strain ellipsoid shows that the stiffest direction ($\varepsilon3$) lies on (010), it is perpendicular to the softest one and is likely governed by the presence of (almost uncompressible) edge-sharing *M3–M1–M3* clusters of octahedra (almost parallel to $\varepsilon3$), connected to the *A2* sites (Fig. 1, Table S2);
(2) The intermediate one ($\varepsilon2$) is parallel to [010]. The compression of the allanite structure along [010] is likely hindered by the presence of the (infinite) edge-sharing $M1O_6$ octahedral chains, running along [010] (Fig. 1, Table S2). Edge-sharing octahedral chains act as "pillars", and the shortening along the chain direction can only occur through intra-polyhedral deformation, by homogeneous or non-homogeneous (i.e., polyhedral distortion) bond-distances compression;
(3) The most compressible direction ($\varepsilon1$, as defined above) in allanite structure lies also on (010). Tilting and compression + distortion of the polyhedra, described above, generate, in turns, the deformations of the 5- and 8-membered rings of polyhedra. The most pronounced compression directions of the rings (represented, e.g. by the diameters $O3 \leftrightarrow O1$ of the 5-membered ring and by $O8 \leftrightarrow O8$ of the 8-membered ring) can play an important role on the orientation of ε1 (Fig. 1, Table S2).

The compressional elastic anisotropy described on the basis of the "linearised bulk moduli" along the three crystallographic axes, all obtained on the basis of a second-order BM-EoS fit (as the truncation to second-order provide the best figures of merit), is $K_{P0,T0}(a)$:$K_{P0,T0}(b)$:$K_{P0,T0}(c)$ = 1.24:1.52:1 in allanite, $K_{T0}(a)$:$K_{T0}(b)$:$K_{T0}(c)$ = 1.13:1.48:1 in epidote with 0.74 Fe a.p.f.u. (recalculated from Gatta et al. 2011b) and $K_{T0}(a)$:$K_{T0}(b)$:$K_{T0}(c)$ = 1:1.19:1.04 in epidote with 0.79 Fe a.p.f.u. (Qin et al. 2016), and $K_{P0,T0}(a)$:$K_{P0,T0}(b)$:$K_{P0,T0}(c)$ = 1:1.81:1.52 in clinozoisite with 0.40 Fe a.p.f.u. (Qin et al. 2016).

The bulk compression of allanite, epidote and clinozoisite is significantly different (Fig. 2). Using a third-order BM-EoS, the following parameters are obtained: $K_{P0,T0}$ = 131(4) GPa and K' = 1.9(8) for allanite, $K_{P0,T0}$ = 111(3) GPa and K' = 7.6(7) for epidote with 0.74 Fe a.p.f.u. (Gatta et al. 2011b) and $K_{P0,T0}$ = 115(2) GPa and K' = 3.7(2) for epidote with 0.79 Fe a.p.f.u. (Qin et al. 2016), and $K_{P0,T0}$ = 142(3) GPa and K' = 5.2(4) for clinozoisite with 0.40 Fe a.p.f.u. (Qin et al. 2016). Epidote is the softest one, clinozoisite is the stiffest and allanite lies in between.

On the basis of a comparative analysis of the compressional behaviour of epidotes and clinozoisites reported in the literature, along with those obtained experimentally in their study, Qin et al. (2016) concluded that increasing Fe content reduces the bulk modulus and increases the first P derivative (using the BM-EoS formulation). This result was attributed to the differences in compression behaviour due to the addition of Fe at the *M3* site (replacing Al) in the epidote structure. Additional in situ HP Raman data collected by Qin et al. (2016) further suggest that the difference in compressibility between epidote and clinozoisite is likely due to the different compressibility of FeO_6– and AlO_6–octahedra, coordinated by the *M3* sites. In allanite, the scenario is more complex: Fe and Al mainly populate the octahedral sites (Fe occurs principally at the *M3* site, like in epidote), but a fraction of Al likely replaces Si at the tetrahedral sites and, more important, Fe along with a series of other LREE elements (mainly Ce and La) replaces

Ca at the *A*1 and *A*2 sites. In this light, the conclusion of Qin et al. (2016), about the role played by iron content on the compressional behaviour, cannot be simplistically extended to allanite, as more variables can influence the different behaviour of allanite if compared to the other two aforementioned members of the epidote group.

Acknowledgements We acknowledge DESY (Hamburg, Germany), a member of the Helmholtz Association HGF, for the provision of experimental facilities. Parts of this research were carried out at PETRA III. GDG, SM, LC, DC, PL, MM acknowledge the support of the Italian Ministry of Education (MIUR) through the project "Dipartimenti di Eccellenza 2018–2022". W. Crichton and an anonymous reviewer are thanked for the revision of the manuscript.

References

Angel RJ (2000) Equation of state. In: Hazen RM, Downs RT (eds) High-temperature and high-pressure crystal chemistry: reviews in mineralogy and geochemistry, vol 41. Mineralogical Society of America and Geochemical Society, Washington, pp 35–59

Angel RJ, Bujak M, Zhao J, Gatta GD, Jacobsen SD (2007) Effective hydrostatic limits of pressure media for high-pressure crystallographic studies. J Appl Crystallogr 40:26–32

Armbruster T, Bonazzi P, Akasaka M, Bermanec V, Chopin C, Gieré R, Heuss-Assbichler S, Liebscher A, Menchetti S, Pan Y, Pasero M (2006) Recommended nomenclature of epidote-group minerals. Eur J Mineral 18:551–567

Birch F (1947) Finite elastic strain of cubic crystal. Phys Rev 71:809–824

Bird DK, Helgeson HC (1980) Chemical interaction of aqueous solutions with epidote-feldspar mineral assemblages in geologic systems, I: thermodynamic analysis of phase relations in the system CaO–FeO–Fe_2O_3–Al_2O_3–SiO_2–H_2O–CO_2. Am J Sci 280:907–941

Bird DK, Cho M, Janik CJ, Liou JG, Caruso LJ (1988) Compositional, order-disorder, and stable isotopic characteristics of Al–Fe epidote, state 2–14 drill hole, Salton Sea geothermal system. J Geophys Res 93(B11):13135–13144

Bonazzi P, Holtstam D, Bindi L, Nysten P, Capitani GC (2009) Multi-analytical approach to solve the puzzle of an allanite-subgroup mineral from Kesebol, Västra Götaland, Sweden. Am Mineral 94:121–134

Catti M, Ferraris G, Ivaldi G (1988) Thermal behaviour of the crystal structure of strontian piemontite. Am Mineral 73:1370–1376

Comodi P, Zanazzi PF (1997) The pressure behaviour of clinozoisite and zoisite. An X-ray diffraction study. Am Mineral 82:61–68

Corti L, Alberelli G, Zanoni D, Zucali M (2017) Analysis of fabric evolution and metamorphic reaction progress at Lago della Vecchia-Valle d'Irogna, Sesia-Lanzo Zone, Western Alps. J Maps 13:521–533

Corti L, Alberelli G, Zanoni D, Zucali M (2018) Tectonometamorphic evolution of the Lago della Vecchia metaintrusive and its country rocks, Sesia-Lanzo Zone, Western Alps. Ital J Geosci 137:188–207

Dollase WA (1971) Refinement of the crystal structure of epidote, allanite and hancockite. Am Mineral 56:447–464

Franz G, Liebscher A (2004) Physical and chemical properties of epidote minerals—an introduction. In: Franz G, Liebscher A (eds) Epidotes: reviews in mineralogy and geochemistry, vol 56. Mineralogical Society of America and Geochemical Society, Washington, pp 1–81

Gatta GD, Meven M, Bromiley G (2010) Effects of temperature on the crystal structure of epidote: a neutron single-crystal diffraction study at 293 and 1,070 K. Phys Chem Minerals 37:475–485

Gatta GD, Alvaro M, Bromiley G (2011a) A low temperature X-ray single-crystal diffraction and polarised infra-red study of epidote. Phys Chem Minerals 39:1–15

Gatta GD, Merlini M, Lee Y, Poli S (2011b) Behavior of epidote at high pressure and high temperature: a powder diffraction study up to 10 GPa and 1200 K. Phys Chem Minerals 38:419–428

Gieré R, Sorensen SS (2004) Allanite and other REE-rich epidote-group minerals. In: Franz G, Liebscher A (eds) Epidotes: reviews in mineralogy and geochemistry, vol 56. Mineralogical Society of America and Geochemical Society, Washington, pp 431–493

Heinz DL, Jeanloz R (1984) The equation of state of the gold calibration standard. J Appl Phys 55:885–893

Holdaway MJ (1972) Thermal stability of Al–Fe epidotes as a function of fO_2 and Fe content. Contrib Min Petrol 37:307–340

Holland TJB, Redfern SAT, Pawley AR (1996) Volume behaviour of hydrous minerals at high pressure and temperature: II. Compressibilities of lawsonite, zoisite, clinozoisite, and epidote. Am Mineral 81:341–348

Klemd R (2004) Fluid inclusions in epidote minerals and fluid development in epidote-bearing rocks. In: Franz G, Liebscher A (eds) Epidotes: reviews in mineralogy and geochemistry, vol 56. Mineralogical Society of America and Geochemical Society, Washington, pp 197–234

Klotz S, Chervin J-C, Munsch P, Le Marchand G (2009) Hydrostatic limits of 11 pressure transmitting media. J Phys D Appl Phys 42:075413 **(7 pp)**

Liebscher A (2004) Spectroscopy of epidote minerals. In: Franz G, Liebscher A (eds) Epidotes: reviews in mineralogy and geochemistry, vol 56. Mineralogical Society of America and Geochemical Society, Washington, pp 125–170

Liou JG (1973) Synthesis and stability relations of epidote, $Ca_2Al_2FeSi_3O_{12}(OH)$. J Petrol 14:381–413

Mao HK, Xu J, Bell PM (1986) Calibration of the ruby pressure gauge to 800 kbar under quasi-hydrostatic conditions. J Geophys Res 91:4673–4676

Pawley AR, Redfern SAT, Holland TJB (1996) Volume behaviour of hydrous minerals at high pressure and temperature: 1. Thermal expansion of lawsonite, zoisite, clinozoisite, and diaspore. Am Mineral 81:335–340

Poli S, Schmidt MW (1998) The high-pressure stability of zoisite and phase relationships of zoisite-bearing assemblages. Contrib Mineral Petrol 130:162–175

Qin F, Wu X, Wang Y, Fan D, Qin S, Yang K, Townsend JP, Jacobsen SD (2016) High-pressure behavior of natural single-crystal epidote and clinozoisite up to 40 GPa. Phys Chem Minerals 43:649–659

Rothkirch A, Gatta GD, Meyer M, Merkel S, Merlini M, Liermann H-P (2013) Single-crystal diffraction at the Extreme conditions beamline P02.2: procedure for collecting and analyzing high-pressure single-crystal data. J Synchrotron Rad 20:711–720

Schmidt MW, Poli S (2004) Magmatic epidotes. In: Franz G, Liebscher A (eds) Epidotes: reviews in mineralogy and geochemistry, vol 56. Mineralogical Society of America and Geochemical Society, Washington, pp 399–430

Sheldrick GM (1997) SHELX-97. Programs for crystal structure determination and refinement. University of Göttingen, Germany

Sheldrick GM (2008) A short history of SHELX. Acta Cryst A64:112–122